

1 **The association between mineralised tissue formation and the mechanical local *in vivo***
2 **environment: Time-lapsed quantification of a mouse defect healing model**

3 Duncan C Tourolle né Betts¹, Esther Wehrle¹, Graeme R Paul¹, Gisela A Kuhn¹, Patrik Christen¹,
4 Sandra Hofmann^{1,2}, Ralph Müller^{1*}

5 ¹ Institute for Biomechanics, ETH Zurich, Zurich, Switzerland, ² Department of Biomedical
6 Engineering and Institute for Complex Molecular Systems, Eindhoven University of Technology,
7 Eindhoven, The Netherlands.

8

9 **Corresponding author:**

10 Ralph Müller, PhD

11 Institute for Biomechanics

12 ETH Zurich

13 Leopold-Ruzicka-Weg 4

14 8093 Zurich, Switzerland

15 Email: ram@ethz.ch

16

17 **Abstract**

18 An improved understanding of how local mechanical stimuli guide the fracture healing process has
19 the potential to enhance clinical treatment of bone injury. Recent preclinical studies of bone defect
20 in animal models have used cross-sectional data to examine this phenomenon indirectly. In this
21 study, a direct time-lapsed imaging approach was used to investigate the local mechanical strains
22 that precede the formation of mineralised tissue at the tissue scale. The goal was to test two
23 hypotheses: 1) the local mechanical signal that precedes the onset of tissue mineralisation is higher
24 in areas which mineralise, and 2) this local mechanical signal is independent of the magnitude of
25 global mechanical loading of the tissue in the defect. Two groups of mice with femoral defects of
26 length 0.85 mm (n=10) and 1.45 mm (n=9) were studied, allowing for distinct distributions of tissue
27 scale strains in the defects. The regeneration and (re)modelling of mineralised tissue was observed
28 weekly using *in vivo* micro-computed tomography (micro-CT), which served as a ground truth for
29 resolving areas of mineralised tissue formation. The mechanical environment was determined using
30 micro-finite element analysis (micro-FE) on baseline images. The formation of mineralised tissue
31 showed strong association with areas of higher mechanical strain (area-under-the-curve: 0.91 ± 0.04 ,
32 true positive rate: 0.85 ± 0.05) while surface based strains could correctly classify 43% of
33 remodelling events. These findings support our hypotheses by showing a direct association between
34 the local mechanical strains and the formation of mineralised tissue.

35 **Introduction**

36 It is accepted that organ-scale mechanical loads have a significant influence on the outcome of bone
37 healing. Yet, at the tissue-scale, where healing takes place, the mechanical stimuli guiding this
38 process are unknown. Manipulation of organ-scale loading has been performed via changes in
39 fixation stiffness and defect size, allowing precise application of load to the defect^{1,2}. Studies
40 focusing on this manipulation of load have shown differential outcomes³. Though understanding of
41 the mechanobiology of bone healing will have profound clinical impact, eventually allowing patient-
42 specific treatment of fractures, a more immediate application of such knowledge might be
43 preclinical research on biomaterials or drugs, via the use of rodent models. In such models, currently
44 a plethora of defect sizes and fixation methods are used⁴. The sensitivity of healing to mechanical
45 stimuli confounds comparisons between studies where: different fixators or defects sizes are used;
46 biomaterials with different stiffnesses are implanted into defects changing the tissue-scale
47 mechanical environment; or pharmaceutical treatments potentially alter the mechanosensitivity of
48 cells. Knowledge of the optimal tissue-scale mechanical conditions would allow compensation for
49 these effects, potentially producing new knowledge on biomaterials and pharmaceutical treatments
50 from existing studies.

51 At the tissue scale several theories have been presented linking mechanical parameters to tissue
52 differentiation such as deviatoric strain and hydrostatic pressure⁵ or shear strain of the tissue and
53 fluid flow within the tissue⁶. However, these theories cannot be confirmed without spatial and
54 temporal experimental data tracking the healing process⁷. In lieu of this, the mechanoregulatory
55 rules have been implemented within *in silico* models and compared to cross-sectional data of the
56 tissue patterning⁸⁻¹⁰. These state-of-the-art *in silico* models are based upon idealised shapes of the
57 tissue; for example, assuming bone is uniform and cylindrical, and the callus extent is predefined.
58 Unfortunately, histological slices rarely conform to these expectations, impeding quantitative
59 comparison¹¹.

60 An alternative to *in silico* modelling is strain mapping where local deformations are estimated using
61 digital images of tissue in the relaxed and deformed states. This method has been used to
62 parametrise and validate finite element (FE) models^{12,13} and also to correlate tissue phenotypes with
63 mechanical strains^{14,15}. While these approaches remove the assumptions used to create finite element
64 models regarding tissue properties, they are sensitive to sample preparation, imaging artefacts and
65 out of plane artefacts given their two dimensionality. Finally, as the data is cross-sectional, the
66 calculated deformation coincides with the tissue compositions but does not precede it.

67 Time-lapsed *in vivo* micro-computed tomography (micro-CT) produces spatial and temporal
68 experimental data for mineralised tissue and, in the field of bone (re)modelling, has enabled non-
69 destructive examination of (re)modelling events over several weeks^{16,17}. When coupled with micro-
70 finite element (micro-FE) analysis, micro-CT imaging, has allowed the investigation of the
71 mechanoregulation of bone (re)modelling¹⁸⁻²⁰. To investigate fracture healing, *in vivo* micro-CT has
72 been used to track changes in bone volume (BV)^{21,22}. Qualitative associations between strain
73 patterns and bone formation have been observed in two dimensional analysis of time-lapsed micro-
74 CT images and FE simulations²¹.

75 In this study, we combine time-lapsed *in vivo* micro-CT with micro-FE analysis to quantify the
76 relationship between the local *in vivo* environment (LivE)²³, bone formation and mineralisation
77 kinetics over the course of healing in a mouse femur defect model. We hypothesize that 1) the
78 tissue-scale mechanical stimulus which precedes the onset of mineralisation is greater in voxels that
79 mineralise than in voxels which do not mineralise and that 2) this phenomenon is independent of the
80 magnitude of global mechanical loading of the defect.

81 Additionally, reconciling the wide range of densities that are observed during the fracture healing
82 process is key to improve micro-FE prediction of mechanical stimuli. Traditionally, either single
83 absolute thresholds, ranging from 394.8 to 641 mg HA/cm³²⁴⁻²⁶ (HA: hydroxyapatite); or relative
84 thresholds based on percentages of grey values; such as 25% to 33%²⁷⁻²⁹ have been used to segment

85 bone. We improve upon these approaches via the use of a “multi-density threshold approach”,
86 whereby we apply a range of thresholds to identify the spatially and temporally changing densities
87 of bone, allowing us to quantify local mineralisation kinetics and reconcile the range of bone
88 densities within the healing environment.

89 **Results**

90 **Longitudinal monitoring of fracture healing**

91 Defect healing followed a typical pattern, progressing from the reparative phase to bridging and then
92 displaying mineralisation and remodelling. The 0.85 mm defect healed in 9/10 mice with the single
93 atrophic non-union which was excluded from analysis. The 1.45 mm defect group had a non-union
94 rate of 4/9, similar to the results of Zwingenberger et al.³⁰. The 0.85 mm group qualitatively had a
95 larger callus compared to the 1.45 mm group (Figure 1). As mentioned before, there is no consensus
96 in literature regarding the level of mineralization for segmenting bone during the healing process.
97 The apparent progression of healing was shown to be highly sensitive to the threshold in both
98 groups. When comparing the highest threshold to the lowest, the peak BV/TV was delayed by at
99 least a week for all regions (Figure 2 a-h). As seen in the formation and resorption rates, two phases
100 of mineralisation could be distinguished (Figure 2 i-p). Firstly, an initial deposition of a large
101 amount of low-density tissue occurred in week 2 and 3, followed by a production decay from the
102 third week onwards; and secondly, an increase in the resorption of low-density tissue and a peak in
103 the formation of high density tissue directly following the first phase (Figure 2 i-p). These results
104 indicate that the production of a lowly mineralized callus and maturation of the tissue are
105 independent processes. The resorption of bone in the FC volumes (Figure 2 k&o) also confirms the
106 results of Schell et al.³¹ who observed osteoclastic activity early in the healing process. Our results
107 indicate that in all VOIs resorption can occur a week after material is deposited, highlighting the
108 substantial overlap between the reparative and remodelling phases.

109 **Estimation of physiological loading**

110 To determine physiological boundary conditions, a load estimation algorithm was used on intact
111 femoral midshafts from a second cohort of mice. The load estimation algorithm predicted an axial
112 compressive load of 10.0 ± 1.9 N with a bending moment of 3.5 ± 0.7 Nmm.

113 **Mechanobiology of tissue mineralisation in the defect**

114 The associations between the effective strain and the mineralisation events in the defect volume
115 were strongest in the second post-operative week, this was true for both groups (Figure 3 a&d). This
116 corresponded with the initiation of hard callus formation (Figure 1 & Figure 2). In both cases, the
117 area under the curve was reduced for the third week and this decrease was proportional to the
118 threshold value. The higher density bone in the third week consisted of both new bone and the
119 maturation of low-density bone deposited in week 2. An AUC of 0.5 implies that maturation was not
120 associated with the mechanical stimuli. This trend is reversed in later weeks, indicating that bone
121 deposited during the remodelling phase is again under mechanical control. For the 0.85 mm group,
122 an effective strain of greater than 0.51 ± 0.25 was found to provoke bone formation, while for the
123 1.45 mm defect the effective strain was 0.85 ± 0.34 . Excluding mice in which non-unions occurred,
124 that effective strain was 0.54 ± 0.26 . While not significant, this may indicate that the non-union mice
125 might have cells that are less mechanically sensitive.

126 The reduction in the effective strain which provoked mineralisation over time (Figure 1, c&f)
127 represents the stress shielding caused by newly formed bone. The effective strain for the 1.45 mm
128 group was lower in week 6 due to the large number of non-unions, which had significantly less
129 strain in the bone tissue.

130 **Mechanobiology of the surface**

131 In order to associate the (re)modelling events on the bone surface with the mechanical stimuli on the
132 surface, the bone surface of the preceding week was extracted from the overlaid binarized images.
133 The state of the surface was recorded, i.e. whether it was a site of formation, resorption or
134 quiescence. The mechanical stimuli were calculated using micro-FE and extracted at the
135 corresponding surface locations. Two thresholds (resorption and formation) were then used to

136 predict the surface state which was then compared to the *in vivo* derived ground truth. Heat plots
137 were generated for each week, mineral density threshold, and VOIs. Only the lower right triangle is
138 occupied as the threshold for resorption and formation cannot overlap. This analysis was performed
139 for all mice in the 0.85 mm group which satisfied the exclusion criteria, using all thresholds and
140 time-points (Figure 5d). In the defect, the CCR in the first 3 weeks was approximately 35-37%, this
141 rose to 40-43% by the 6th week (Figure 4b). In the VOIs of the cortical fragments, the CCR was
142 initially 50-56% decreasing to 39-40% by the 6th week (Figure 4a). At lower mineral density
143 thresholds, for both the defect and cortical fragments, there was a tendency for a higher CCR.
144 Comparing the defect and cortical fragments, it is apparent that the CCRs for both DF+DP and
145 FC+FP approach the same value in the final week (Figure 4).

146 **Discussion**

147 The aim of this study was to investigate the mechanical regulation of bone healing in the local *in*
148 *vivo* environment (*LivE*) and determine if the tissue-scale stimulus preceding formation of
149 mineralised tissue was independent of global loading of the defect. Our first hypothesis, that the
150 formation of mineralised tissue during bone healing is regulated, at least partly, by tissue scale
151 mechanical stimuli could be confirmed, with up to 91±3.4% of mineralised tissue formation within
152 the defect being predicted by a single threshold for both defect sizes (Figure 3). The lack of a
153 significant difference between the optimal ε_{eff} during the 2nd week post-operative measurement of
154 the 0.85mm and 1.45mm defect groups further strengthens this finding and means that we cannot
155 reject the second hypothesis.

156 While previous studies have focused on qualitative assessment of the mechanoregulation²¹, or on
157 two dimensional cross-sectional data^{5,10,15}, this study uses fully three dimensional information and
158 associates a preceding strain with the tissue. In our study, we focused on ε_{eff} as a classifier. The
159 choice of ε_{eff} rather than SED is due to the heterogenous nature of the tissues in the healing bone.
160 As SED scales linearly with stiffness, this precluded comparison between regions with different
161 Young's moduli. In contrast, ε_{eff} is independent of the element elasticity. Previous studies have

162 attempted to divide the mechanical stimuli into either shear and volumetric components or the
163 perfusion of fluid through the tissue matrix and shear^{5,6}. However, adversarial testing by Repp et
164 al.¹⁰ could not falsify any proposed theory. Nevertheless, Repp et al. found that a simple model
165 using only volumetric strain could produce an equivalent healing outcome. In contrast, Epari et al.³²
166 stated that deviatoric strains dominated the mechanoregulation in their studies. The difference
167 between Epari et al. and Repp et al. might be explained by the different dominant modes of loading:
168 shear versus compression. Our use of ε_{eff} combines both deviatoric strains and volumetric strains
169 into a single scalar quantity. As SED has been used extensively for the analysis of bone
170 (re)modelling, using a derived quantity can allow for a unifying theory of both bone repair and
171 (re)modelling.

172 When considering (re)modelling, the association of (re)modelling events at the surface is
173 comparable to Schulte et al.³³, who were able to predict the spatial accuracy of formation and
174 resorption (equivalent to CCR) at 47.6 % (SD=3.3 %) in caudal vertebrae of mice compared to the
175 CCR of 42% (SD=2.4 %) in this study. The surface (re)modelling events of the cortical bone
176 initially had a strong association with the mechanical stimuli when compared to bone in the defect.
177 The CCR of cortical bone decreased over the study period, converging with the CCR of the defect
178 (Figure 4). We see two potential explanations for this behaviour: Firstly, the cortical VOIs were
179 inactive during the first week (Figure 2 k&l). Thus, most of the surface was in a quiescent state with
180 a small amount of bone resorption. This reduced the total amount of possible misclassifications as
181 the ground truth has two states rather than three. The amount of (re)modelling activity then
182 increased in the subsequent weeks, hence the CCR decreased as the surface enters a state of
183 balanced remodelling where the amount of newly formed bone is equal to the resorbed bone.
184 Secondly, it is possible that errors in our boundary conditions were lower for the non-healed bone
185 when the majority of load was transmitted through the external fixator and boundary artefacts
186 relating to the screws were lower. In the coarse FE-model, the entire callus is modelled as a
187 homogenous material where the boundary conditions are related to the *in vivo* micro-FE model

188 based purely upon the axial stiffness of the callus. The bending stiffness of the callus is not
189 controlled in either model and is a source of error.

190 There were several limitations related to this work. The following assumptions were made in our FE
191 models regarding material properties: (i) all materials are linear elastic, (ii) all materials have a
192 homogenous Poisson's ration of 0.3, (iii) all voxels not containing bone have a homogenous
193 stiffness of 3 MPa, and (iv) the boundary conditions are estimated. Regarding limitations (i) and (ii),
194 the first two assumptions are constrained by model size. The largest model had approximately 102
195 million degrees of freedom and to solve these models in a reasonable amount of time and have a
196 manageable amount of data, we relied upon the linear elastic micro-FE solver ParOSol³⁴. ParOSol
197 has the restriction that all elements have the same Poisson's ratio. Steiner et al.¹³ used electro
198 speckle interferometry to strain map sections of calluses to assess the Poisson's ratio of tissues in a
199 healing callus, and while they found high variance in the locally assessed Poisson's ratio, the
200 average Poisson's ratios of cartilage and bone were 0.3, indicating that our assumption is in line with
201 the literature. Regarding assumption (iii), using our micro-CT imaging protocol, it was only possible
202 to differentiate mineralised tissue from non-mineralised tissue. Therefore, the development of soft
203 tissues and their association with the mechanical stimulus was not quantified. Incorporation of MRI
204 data for comparable fixator stiffness and defect size, such as that captured by Haffner-Luntzer et
205 al.³⁵, would allow our analysis to include cartilage formation and more detailed mechanical stimulus
206 in the soft tissue region. Finally considering assumption (iv), the physiological loading of the mouse
207 hind limb is currently unknown. Although a musculoskeletal model of the mouse hind limb has been
208 developed by Charles et al.³⁶, this has not been validated or applied to mouse gait data. Charles et al.
209 calculated the maximum moments exerted on a mouse femur. The muscle M. psoas major induces a
210 peak flexion moment of 3 Nmm on the femur. This muscle is inserted into the femur at
211 approximately the same level as the boundary of the micro-FE model used for load estimation. This
212 moment is comparable to the 3.5 ± 0.7 Nmm we calculated using a load estimation algorithm. The

213 prediction of such similar values with two different methodologies lends confidence to the predicted
214 physiological loading presented in this paper.

215 In summary, we investigated the association between formation of mineralised tissue and the local
216 mechanical stimuli over the course of healing in a mouse femoral defect model. The results indicate
217 that the bone healing process is mechanically regulated at the tissue-scale in the reparative phase.
218 These results also provide both parameters and ground truth to improve and validate fracture healing
219 models in mice. Combinations of the methods presented will reduce animal numbers needed in bone
220 healing studies, through longitudinal monitoring, and allow quantification of mineralisation kinetics
221 and mechanosensitivity. Finally, knowledge of mechanical stimuli at the tissue-scale will allow
222 mouse studies to choose the fixation stiffness and defect sizes which tailor the local mechanical
223 environments to physiologically relevant ranges.

224 **Material and Methods**

225 **Animal model and imaging**

226 All animal procedures were approved by the authorities (licence number: 36/2014; Kantonales
227 Veterinäramt Zürich, Zurich, Switzerland). We confirm that all methods were carried out in
228 accordance with relevant guidelines and regulations (ARRIVE guidelines and Swiss Animal
229 Welfare Act and Ordinance (TSchG, TSchV)). The study comprised of two groups of female
230 C57BL/6J mice, age 20 ± 1 week (Janvier Laboratories, Le Genest-Saint-Isle, France). In both
231 groups, a femoral defect was created by first stabilising the femur with a radio-translucent external
232 fixator (MouseExFix, RISystem AG, Davos, Switzerland) and then removing a section of bone. One
233 group ($n=10$) received a 0.85 ± 0.09 mm defect. The second group ($n=9$) consisted of animals from an
234 existing study³⁷, which had a 1.45 ± 0.16 mm defect. The mice were scanned weekly using *in vivo*
235 micro-CT (vivaCT 40, Scanco Medical AG, Brütisellen, Switzerland) with an energy of 55 kVp, an
236 integration time of 350 ms and a current of 145 μ A with 500 projections. The scanning period was 6
237 weeks, totalling 7 measurements, including a post-operative scan. To prevent motion artefacts
238 during scanning, the external fixator was secured in a custom designed holder. During all

239 experimental procedures, the animals underwent isoflurane anaesthesia (Induction: 5%, maintenance
240 2-3%). Analgesia (Tramadol, 25 mg/l; Tramal[®], Gruenthal GmbH, Aachen, Germany) was
241 provided via the drinking water during the peri-operative period (two days before surgery until the
242 third postoperative day). Atrophic non-unions, qualitatively assessed in the micro-CT scans, served as
243 an exclusion criterion.

244 **Image processing**

245 Three dimensional micro-CT images were reconstructed at an isotropic nominal resolution of 10.5
246 μm . Images were registered sequentially; proximal and distal bone fragments of unbridged defects
247 were registered separately as it was found that small relative movements between proximal and
248 distal bone fragments occurred between measurements, the registration used the algorithm described
249 by Schulte et al.¹⁷. After image registration, the images were Gaussian filtered (sigma 1.2, support 1)
250 to reduce noise. The multi-density threshold approach was then applied, whereby images were
251 binarized with thresholds ranging from 395 to 720 mg HA/cm³ in steps of 25 mg HA/cm³. The
252 threshold of 395 mg HA/cm³ corresponded to the lowest value used to segment bone in existing
253 studies²⁵. The highest threshold was chosen as it allowed the threshold range to encompass 640 mg
254 HA/cm³, the highest value found in the literature²⁴.

255 The bone volume was evaluated in four non-overlapping volumes of interest (VOIs) which were
256 created from the post-operative measurement. These consisted of a defect centre (DC), defect
257 periphery (DP), a volume encompassing each both cortical fragments (FC), and the fragment
258 periphery (FP) (Figure 5a). These volumes were identified automatically using the following
259 algorithm: The input was the post-operative image binarized with a threshold of 645 mg HA/cm³,
260 which was chosen because it disconnected surgical debris from the cortical fragments. The cortical
261 fragments were found using component labelling. The marrow cavities on each side were flood
262 filled, creating the FC VOI. The cortical surface was taken from the last filled slice of the FC mask
263 and interpolated linearly across the defect. A raytracing approach was implemented, where rays
264 were cast from the image boundaries perpendicular to the axis joining the centre of mass of the

265 cortical fragments. If the ray struck a cortical fragment (Figure 5a) all voxels along its path were
266 included in the FP VOI, while if the ray struck the interpolated surface the voxels were then added
267 to the DP VOI (Figure 5a). The DC VOI was then determined as the voxel in the image not included
268 in the FC, FP and DP VOIs. The bone volume was quantified for all thresholds. The volumes were
269 normalised to the central VOIs, DC for DP and FC for FP representing the total volume (TV) of
270 intact bone, which can be considered as a target for healing.

271 **Finite element analysis**

272 The mechanical signal was calculated using three hierarchical FE analyses; 1) Load estimation was
273 used to determine the physiological loading on the intact mouse femur (Figure 5b), 2) A coarse
274 finite element model of the bone-fixator system was used to determine the boundary conditions of
275 the femoral defect (Figure 5b), and 3) a micro-FE analysis based upon the *in vivo* micro-CT images
276 was used to estimate the tissue-scale mechanical stimuli (Figure 5c&d).

277 **Load estimation.**

278 The physiological loading of the mouse femur was determined using a load estimation method
279 proposed by Christen et al.³⁸. This method uses the underlying microstructure of the bone to
280 determine a combination of load cases, which create a homogenous strain distribution at a
281 physiological tissue loading level.

282 The loading parameters were estimated from images of intact contralateral femurs of a second
283 cohort of seven female mice (C57BL/6J) from a previously published fracture healing study³⁹.
284 Samples were scanned and processed *ex vivo* in a desktop micro-CT system (microCT 40, Scanco
285 Medical AG, Brüttisellen, Switzerland) according to the protocol established by Kohler et al.⁴⁰. The
286 mid-shaft was extracted manually as the region above the lower growth plate and below the lesser
287 trochanter. Two load cases with unitary loads were applied to the mid-shafts: axial compression and
288 a bending moment around the minor axis of ellipticity of the femoral cross-section (Fig 5b). The
289 micro-FE analyses for each load condition were then solved using ParOSol³⁴, using a 1:1 conversion

290 of voxels to elements. The load estimation algorithm was then used to determine the physiological
291 loading applied to the shaft.

292 **Coarse finite element model**

293 To translate the organ-scale loads to the tissue-scale in the *in vivo* micro-CT model, a coarse finite
294 element model was created containing the external fixator and the femoral mid-shaft. The central
295 section of the mid-shaft was replaced with a material representative of the *in vivo* micro-CT model.
296 The model was solved using ABAQUS V6.11 (Dassault systems, Vélizy-Villacoublay, France). The
297 boundary conditions consisted of the load and bending moment determined using the load
298 estimation. All elements were linear elastic, bone stiffness was 14.8 GPa and a Poisson's ratio of 0.3
299 was used⁴¹. The femoral mid-shaft was modelled as elliptical tubes, with a thickness of 0.2 mm and
300 a minor and major axis of 1.0 mm and 2.0 mm respectively. The fixator was modelled on the
301 MouseExFix system used in the study. The model of the entire system consisted of approximately
302 250,000 elements. The validity of this model was verified through comparing the simulated stiffness
303 to mechanical compression experiments of the external fixator implanted into PMMA cylinders with
304 an empty defect (Supplementary Fig. S1 and Supplementary Table S1).

305 **Estimation of *in vivo* strains**

306 For each mouse and time-point a micro-FE model was created. Each model combined the
307 thresholded images, where HA-equivalent mineral densities were converted to a Young's modulus
308 using a linear relationship^{42,43} with a value of 14 GPa corresponding to 720 mg HA/cm³, the highest
309 level of density segmented, while 395 mg HA/cm³ corresponded to 4 GPa. The background of the
310 image was given a value of 3.0 MPa to represent soft tissue⁴⁴. The stiffness of the defect was
311 determined by applying a simple compression of 1% displacement to the cortical bone and the
312 marrow cavity. Using the coarse model, physiological displacements at the image edges could be
313 determined and applied as boundary conditions. The mechanical stimulus used was effective strain
314 was calculated as described by Pistoia et al.⁴⁵. The micro-FE models consisted of approximately 25
315 million elements, totalling 75 million degrees of freedom, which were solved with the parallel solver

316 ParOSol³⁴. Simulations were run on Piz Daint, a Cray XC30/40 system at the Swiss National Centre
317 (CSCS), utilising 8 nodes and 144 cores with a solution time of approximately 5 minutes per
318 analysis.

319 **Analysis of mechanobiology of bone healing**

320 To associate bone formation with the mechanical stimuli within the defect, a receiver operating
321 characteristic analysis (ROC) was applied (Figure 5c). In our application of ROC, the ground truth
322 was created by overlaying binarized images where newly mineralised bone was identified as
323 condition positive, while tissue which did not mineralise was condition negative. The ROC curve
324 was created via sweeping a threshold through the ε_{eff} space, values above the strain threshold were
325 classified as bone while below were considered soft tissue. The comparison to the ground truth
326 created the ROC curve (Figure 5c). The analysis was performed in the DC and DP volumes. This
327 process was repeated for each mouse, time-point and mineral density threshold. Due to the large
328 amount of data, the analysis was summarised in terms of area under the curve and the true positive
329 rate selected was the furthest from the random classification line at 45°.

330 **Analysis of mechanobiology of callus remodelling**

331 On the bone surface, the prediction of sites of formation, resorption and quiescence using the
332 preceding effective strain was interpreted as a multi-class classification problem. The classifier
333 function f_j consisted of two thresholds, as shown in equation (1). The lower threshold classified the
334 sites of resorption (T_R), and an upper threshold classified the sites of formation (T_F), values between
335 the thresholds were classified as quiescent.

$$Signal > T_F \rightarrow f_F(Signal) = True$$

$$Signal < T_F \rightarrow f_F(Signal) = False$$

$$336 \quad Signal > T_R \rightarrow f_R(Signal) = False \quad (1)$$

$$Signal < T_R \rightarrow f_R(Signal) = True$$

$$T_R < Signal < T_F \rightarrow f_Q(Signal) = True$$

337 This classifier corresponds to the simplest possible mechanostat model, having just two parameters
338 (T_R and T_F)⁴⁶.

339 The bone surface was defined as the interface between the bone and the background using a 3D ‘von
340 Neumann’ neighbourhood with a radius of 1 voxel⁴⁷. The ground truth G was determined with sites
341 of formation defined as the interface between quiescent and newly formed bone. Sites of resorption
342 were defined as the interface between resorbed bone and the background, while the quiescent
343 surface was the interface between quiescent bone and the background. The predicted states were
344 then compared to the ground truth and a category-wise normalised confusion matrix C , equation (2),
345 was generated.

$$346 \quad C_{ij} = \frac{1}{\sum G_j} \sum G_j(x) \cap f_j(S(x)) \quad (2)$$

347 Diagonal entries are analogous with true positive rate, while off diagonals are false negatives and
348 positives. The trace of the normalised confusion matrix indicates the overall performance for all
349 categories. The normalisation step compensates for differences in the number of surface voxels in
350 each category (formation, quiescence and resorption), and thus gives all events equal weighting. An
351 exhaustive analysis comparable to ROC was performed in which both thresholds were swept
352 through the strain space generating two dimensional heat charts (Fig 5d). The colour represents the
353 trace of the confusion matrix divided by three to give an average correct classification rate (CCR),
354 as described in equation (3).

$$355 \quad CCR = \frac{1}{N_{states}} \sum_{i=1}^{N_{states}} C_{ii} \quad (3)$$

356 This analysis was performed for each mineral density threshold level, and the maximum CCR was
357 determined for each image and time-point.

358 **Data availability**

359 All necessary data generated or analyzed during the present study are included in this published
360 article and its Supplementary Information files (preprint available on BioRxiv/2019/721365).
361 Additional information related to this paper may be requested from the authors.

362 **References**

- 363 1. Goodship, A., Watkins, P., Rigby, H. & Kenwright, J. The role of fixator frame stiffness in the
364 control of fracture healing. An experimental study. *J. Biomech.* **26**, 1027–1035 (1993).
- 365 2. Schell, H. *et al.* The course of bone healing is influenced by the initial shear fixation stability. *J.*
366 *Orthop. Res.* **23**, 1022–1028 (2005).
- 367 3. Betts, D. C. & Müller, R. Mechanical Regulation of Bone Regeneration: Theories, Models, and
368 Experiments. *Front. Endocrinol. (Lausanne)*. **5**, (2014).
- 369 4. Harris, J. S., Bemenderfer, T. B., Wessel, A. R. & Kacena, M. A. A review of mouse critical
370 size defect models in weight bearing bones. *Bone* (2013).
- 371 5. Claes, L. & Heigele, C. Magnitudes of local stress and strain along bony surfaces predict the
372 course and type of fracture healing. *J. Biomech.* **32**, 255–266 (1999).
- 373 6. Prendergast, P., Huiskes, R. & Søballe, K. Biophysical stimuli on cells during tissue
374 differentiation at implant interfaces. *J. Biomech.* **30**, 539–548 (1997).
- 375 7. Geris, L., Vander Sloten, J. & Van Oosterwyck, H. In silico biology of bone modelling and
376 remodelling: regeneration. *Philos. Trans. Royal Soc. A*. **367**, 2031–2053 (2009).
- 377 8. Lacroix, D. & Prendergast, P. A mechano-regulation model for tissue differentiation during
378 fracture healing: analysis of gap size and loading. *J. Biomech.* **35**, 1163–1171 (2002).
- 379 9. Burke, D. P. & Kelly, D. J. Substrate stiffness and oxygen as regulators of stem cell
380 differentiation during skeletal tissue regeneration: a mechanobiological model. *PLoS One* **7**,
381 e40737 (2012).
- 382 10. Repp, F., Vetter, A., Duda, G. N. & Weinkamer, R. The connection between cellular
383 mechanoregulation and tissue patterns during bone healing. *Med. Biol. Eng. Comput.* **53**, 829–
384 842 (2015).
- 385 11. Vetter, A., Witt, F., Sander, O., Duda, G. & Weinkamer, R. The spatio-temporal arrangement of
386 different tissues during bone healing as a result of simple mechanobiological rules. *Biomech.*
387 *Model. Mechanobiol.* **11**, 147–160 (2012).
- 388 12. Bottlang, M., Mohr, M., Simon, U. & Claes, L. Acquisition of full-field strain distributions on
389 ovine fracture callus cross-sections with electronic speckle pattern interferometry. *J. Biomech.*
390 **41**, 701–705 (2008).
- 391 13. Steiner, M., Claes, L., Simon, U., Ignatius, A. & Wehner, T. A computational method for
392 determining tissue material properties in ovine fracture calluses using electronic speckle pattern
393 interferometry and finite element analysis. *Med. Eng. Phys.* **34**, 1521–1525 (2012).
- 394 14. Morgan, E. F. *et al.* Correlations between local strains and tissue phenotypes in an experimental
395 model of skeletal healing. *J. Biomech.* **43**, 2418–2424 (2010).
- 396 15. Miller, G. J., Gerstenfeld, L. C. & Morgan, E. F. Mechanical microenvironments and protein
397 expression associated with formation of different skeletal tissues during bone healing. *Biomech.*
398 *Model. Mechanobiol.* **14**, 1239–1253 (2015).
- 399 16. Schulte, F. A., Lambers, F. M., Mueller, T. L., Stauber, M. & Müller, R. Image interpolation
400 allows accurate quantitative bone morphometry in registered micro-computed tomography
401 scans. *Comput. Methods Biomech. Biomed. Engin.* **17**, 539–548 (2014).
- 402 17. Schulte, F. A., Lambers, F. M., Kuhn, G. & Müller, R. In vivo micro-computed tomography
403 allows direct three-dimensional quantification of both bone formation and bone resorption
404 parameters using time-lapsed imaging. *Bone* **48**, 433–442 (2011).

- 405 18. Webster, D., Schulte, F. A., Lambers, F. M., Kuhn, G. & Müller, R. Strain energy density
406 gradients in bone marrow predict osteoblast and osteoclast activity: a finite element study. *J.*
407 *Biomech.* **48**, 866–874 (2015).
- 408 19. Christen, P. *et al.* Bone remodelling in humans is load-driven but not lazy. *Nat. Commun.* **5**,
409 4855 (2014).
- 410 20. Christen, P. & Müller, R. In vivo visualisation and quantification of bone resorption and bone
411 formation from time-lapse imaging. *Curr. Osteoporos. Rep.* **15**, 311–317 (2017).
- 412 21. Mehta, M., Checa, S., Lienau, J., Hutmacher, D. & Duda, G. N. In vivo tracking of segmental
413 bone defect healing reveals that callus patterning is related to early mechanical stimuli. *Eur.*
414 *Cell. Mater.* **24**, 71 (2012).
- 415 22. Tsitsilonis, S. *et al.* The effect of traumatic brain injury on bone healing: an experimental study
416 in a novel in vivo animal model. *Injury* **46**, 661–665 (2015).
- 417 23. Trüssel, A., Flohr, F., Kuhn, G. A. & Müller, R. Gene expression and local in vivo environment
418 (LivE) imaging of osteocyte subpopulations in trabecular mouse bone. *J. Bone. Miner. Res.*
419 **30(S1):S100**, (2015).
- 420 24. Morgan, E. F. *et al.* Micro-computed tomography assessment of fracture healing: relationships
421 among callus structure, composition, and mechanical function. *Bone* **44**, 335–344 (2009).
- 422 25. O’Neill, K. R. *et al.* Micro-computed tomography assessment of the progression of fracture
423 healing in mice. *Bone* **50**, 1357–1367 (2012).
- 424 26. Locher, R. *et al.* Traumatic brain injury and bone healing: radiographic and biomechanical
425 analyses of bone formation and stability in a combined murine trauma model. *J. Musculoskelet.*
426 *Neuronal. Interact.* **15**, 309–315 (2015).
- 427 27. Gardner, M. J. *et al.* Differential fracture healing resulting from fixation stiffness variability: a
428 mouse model. *J. Orthop. Sci.* **16**, 298–303 (2011).
- 429 28. Weis, J. A. *et al.* Comparison of microCT and an inverse finite element approach for
430 biomechanical analysis: Results in a mesenchymal stem cell therapeutic system for fracture
431 healing. *J. Biomech.* (2012).
- 432 29. Freeman, T. A., Patel, P., Parvizi, J., Antoci, V. & Shapiro, I. M. Micro-CT analysis with
433 multiple thresholds allows detection of bone formation and resorption during ultrasound-treated
434 fracture healing. *J. Orthop. Res.* **27**, 673–679 (2009).
- 435 30. Zwingenberger, S. *et al.* Establishment of a femoral critical-size bone defect model in
436 immunodeficient mice. *J. Surg. Res.* **181**, e7–e14 (2013).
- 437 31. Schell, H. *et al.* Osteoclastic activity begins early and increases over the course of bone healing.
438 *Bone* **38**, 547–554 (2006).
- 439 32. Epari, D. R., Taylor, W. R., Heller, M. O. & Duda, G. N. Mechanical conditions in the initial
440 phase of bone healing. *Clin. Biomech.* **21**, 646–655 (2006).
- 441 33. Schulte, F. A. *et al.* Strain-adaptive in silico modeling of bone adaptation: A computer
442 simulation validated by in vivo micro-computed tomography data. *Bone* **52**, 485–492 (2013).
- 443 34. Flaig, C. A highly scalable memory efficient multigrid solver for μ -finite element analyses.
444 (2012).
- 445 35. Haffner-Luntzer, M. *et al.* Evaluation of high-resolution In Vivo MRI for longitudinal analysis
446 of endochondral fracture healing in mice. *PLoS One* **12**, e0174283 (2017).
- 447 36. Charles, J. P., Cappellari, O., Spence, A. J., Wells, D. J. & Hutchinson, J. R. Muscle moment
448 arms and sensitivity analysis of a mouse hindlimb musculoskeletal model. *J. Anat.* (2016).
- 449 37. Wehrle, E. *et al.* Evaluation of longitudinal time-lapsed in vivo micro-CT for monitoring
450 fracture healing in mouse femur defect models. *Sci. Rep.* 10.1038/s41598-019-53822-x (2019).
- 451 38. Christen, P., Ito, K., Galis, F. & van Rietbergen, B. Determination of hip-joint loading patterns
452 of living and extinct mammals using an inverse Wolff’s law approach. *Biomech. Model.*
453 *Mechanobiol.* **14**, 427–432 (2015).
- 454 39. Wehrle, E. *et al.* In vivo micro-CT based approach for discrimination of physiological and
455 impaired healing patterns in mouse femur defect models. *Eur. Cell. Mater.* **31**, (2016).

- 456 40. Kohler, T., Stauber, M., Donahue, L. R. & Müller, R. Automated compartmental analysis for
457 high-throughput skeletal phenotyping in femora of genetic mouse models. *Bone* **41**, 659–67
458 (2007).
- 459 41. Webster, D. J., Morley, P. L., van Lenthe, G. H. & Müller, R. A novel in vivo mouse model for
460 mechanically stimulated bone adaptation—a combined experimental and computational validation
461 study. *Comput. Methods Biomech. Biomed. Engin.* **11**, 435–441 (2008).
- 462 42. Mulder, L., Koolstra, J. H., den Toonder, J. M. J. & van Eijden, T. M. G. J. Intratrabecular
463 distribution of tissue stiffness and mineralization in developing trabecular bone. *Bone* **41**, 256–
464 65 (2007).
- 465 43. Shefelbine, S. J. *et al.* Prediction of fracture callus mechanical properties using micro-CT
466 images and voxel-based finite element analysis. *Bone* **36**, 480–488 (2005).
- 467 44. Simon, U., Augat, P., Utz, M. & Claes, L. A numerical model of the fracture healing process
468 that describes tissue development and revascularisation. *Comput. Methods Biomech. Biomed.*
469 *Engin.* **14**, 79–93 (2011).
- 470 45. Pistoia, W. *et al.* Estimation of distal radius failure load with micro-finite element analysis
471 models based on three-dimensional peripheral quantitative computed tomography images. *Bone*
472 **30**, 842–848 (2002).
- 473 46. Frost, H. M. Bone “mass” and the “mechanostat”: a proposal. *Anat. Rec.* **219**, 1–9 (1987).
- 474 47. Schulte, F. A. *et al.* Local mechanical stimuli regulate bone formation and resorption in mice at
475 the tissue level. *PLoS One* **8**, e62172 (2013).

476

477

478 **Acknowledgements**

479 The authors gratefully acknowledge funding from the European Union (BIODESIGN FP7-NMP-
480 2012-262948) and computational time from the Swiss National Supercomputing Centre (CSCS). E.
481 Wehrle received funding from the ETH Postdoctoral Fellowship Program (MSCA-COFUND, FEL-
482 25_15-1).

483 **Author contributions**

484 The study was designed by D.C.T, E.W, G.A.K, S.H and R.M. The experiments were performed by
485 E.W, G.R.P and G.A.K. Data analyses were performed by D.C.T. Interpretation of the data was
486 performed by D.C.T, E.W, G.R.P, G.A.K, P.C and R.M. The manuscript was written by D.C.T and
487 reviewed and approved by all authors.

488 **Competing Interests**

489 The authors declare no competing interests.

490

491 **Figure Legends**

492 Figure 1. Callus development over the course of the study for both 0.85 mm and 1.45 mm defects.
493 Two thresholds are shown for each mouse, most significant is the difference between observed state
494 of healing at week 2, where for the lower threshold both groups are fused and for the higher
495 threshold no healing has occurred.

496

497 Figure 2. The development and kinetics of mineralised tissue in the defect. a-h show the time course
498 of bone volume. i-p shows the mineralisation kinetics, resorption and formation are separated. The
499 mean of the 0.85mm, panels a-d and i-l, and mean of 1.45 mm, panels e-f and m-f. Note that as a
500 proportion of the defect more tissue is formed within the 0.85mm group compared to the 1.45mm
501 group. A successful healing outcome is a union in which the bone is indistinguishable from the
502 original cortical bone, comparing the original cortical fragments FC+FP and defect VOIs DC+DP
503 between groups, it is apparent that the 0.85mm defect has similar BV/TV in the DC+DP (a+b) and
504 FC+FP (c+d) in the final weeks, while the 1.45mm defect groups has lower BV/TV within the DC
505 and DP regions. This shows that insufficient bone is produced in the larger defect. For both groups
506 the difference between the highest and lowest threshold would cause relative underestimation of
507 callus size in the initial 3 post-operative weeks. The rates of mineralisation were threshold
508 dependent, with an initial large deposit of lowly mineralised tissue followed by a second phase of
509 maturation a-h. Resorption of the existing cortical fragments was apparent in week 1-3.

510

511 Figure 3. The associations between mineralisation on the mechanical local *in vivo* environment:
512 Time course of area under curve (AUC) (a,d), True positive rate (b,e) and Effective Strain thresholds
513 (c,f) for 0.85 mm (upper row) and 1.45 mm (lower row) defects. a,d) The area under curve for the
514 0.85 mm and 1.45 mm respectively. In both groups the AUC was maximum in the second week. The
515 AUC declined in the third week for both groups, this decline was largest for the highest mineralised
516 tissue, again recovering for the 0.85 mm, while continuing to decline for the 1.45 mm group. The

517 poor association between the formation of highly mineralised tissue and mechanical signal in the
518 third week is an indication that the maturation of bone is independent of the local mechanics while
519 its formation is dependent. The recovery of the AUC in the later weeks for the 0.85 mm is likely due
520 to the group containing only mice with unions. The true positive rate of the optimal threshold (b,e),
521 initially show a similar trend to the AUC. However, for the 0.85 mm group the association for the
522 highest mineral density threshold is also highest in the final week, indicating that controlled
523 remodelling is taking place. The optimal effective strain thresholds (c,f) show a similar level of
524 strain in the second week. A large amount of variation with respect to mineral density threshold can
525 be seen in the 1.45 mm group from week 3 onwards, which is likely due to the presence of both
526 unions (which stress shield soft tissue) and non-unions in the group.

527 Figure 4. The highest mean correct classification rates for remodelling events for each week and
528 mineralisation threshold. a) Remodelling events in the fragment VOIs, showing a drop in CCR as
529 the cortices shift from resorption to balanced remodelling. b) Remodelling events in the defect,
530 initially close to random followed by an increase each week post bridging.

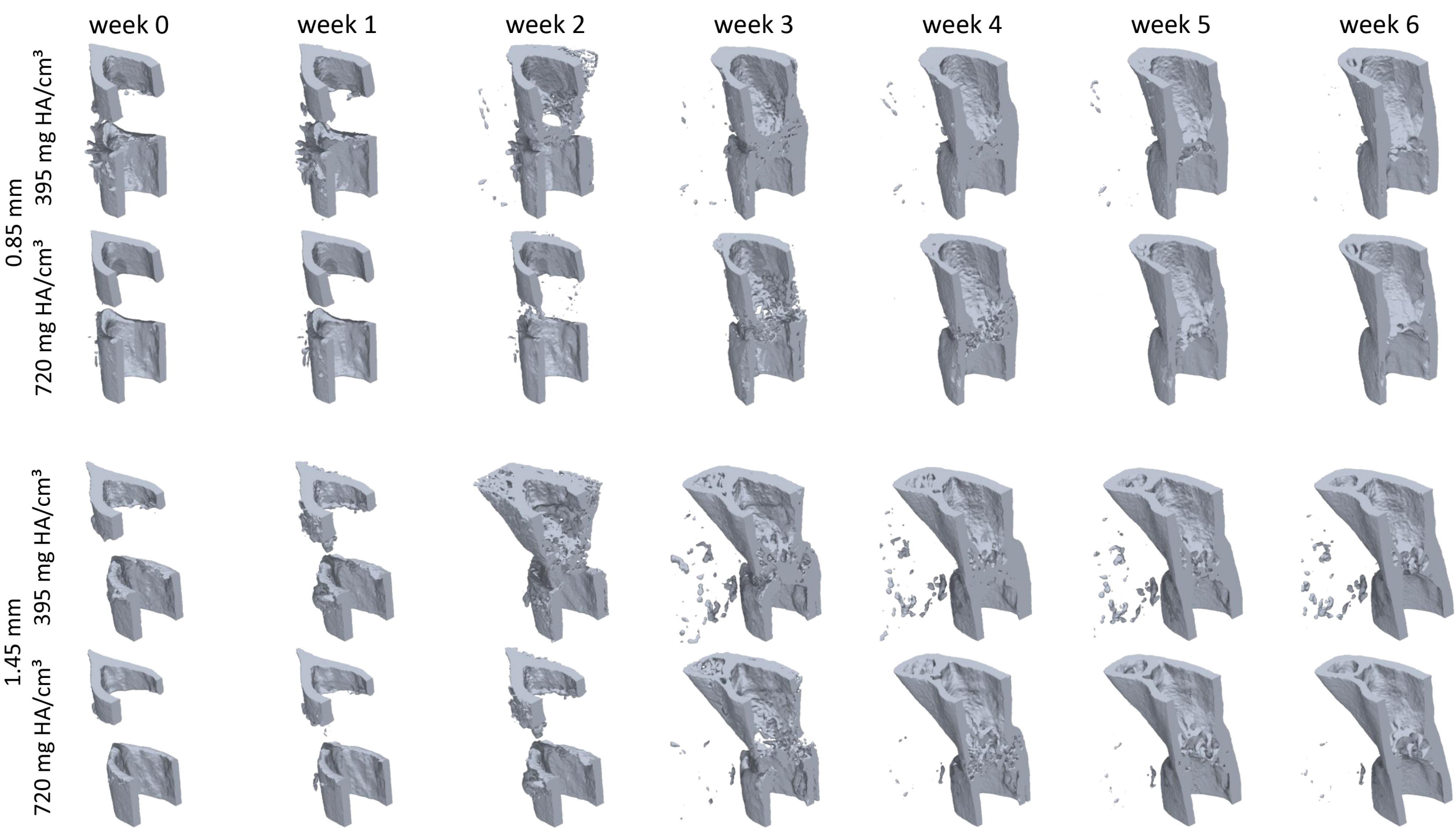
531

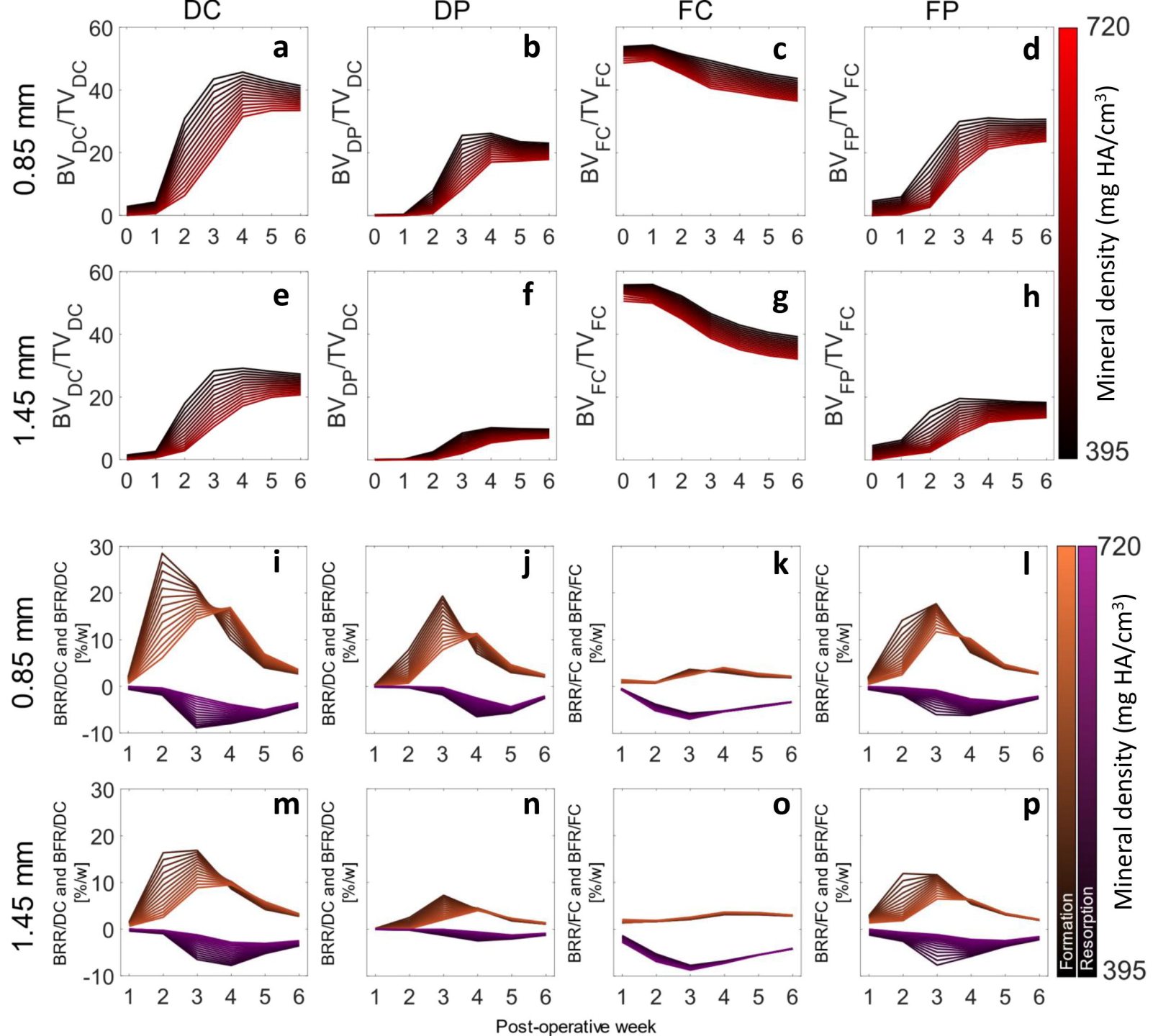
532 Figure 5. a) Illustration of ROI definition process: First the first and last intact cortical slice in the
533 imaging plane are found (proximal blue, distal red). These shapes are then interpolated across the
534 defect, providing an estimation of the original periosteum. Rays are then cast from the image
535 boundaries along normals to the major axis of the fragments. Rays which intersect the cortical
536 fragments are classified as being members of FP, while rays which intersects only virtual periosteal
537 surface (red) are classified as being in DP. The DC volume is then determined as the space not
538 occupied by FC, FP or DP. b) The pipeline for FE analysis: initially the load on the femur was
539 determined using load estimation on intact contralateral femurs. These loads were then applied to a
540 coarse FE-model which determined the boundary conditions for the *in vivo* micro-CT model. c) The
541 association between mineralised tissue formation and mechanical strain in the soft tissue, micro-FE

542 analysis is used to calculate the strains in the soft tissue, using the time-lapsed *in vivo* micro-CT
543 images as ground truth ROC analysis is performed determining how effective mechanical strain is as
544 a predictor. d) Association of remodelling events with mechanical strain. Using the micro-FE results
545 for the mineralised tissue a set of thresholds are swept through the strain space classifying formation
546 and resorption events. Using the time-lapsed *in vivo* micro-CT images as ground truth, a correct
547 classification rate for each set of thresholds is determined.

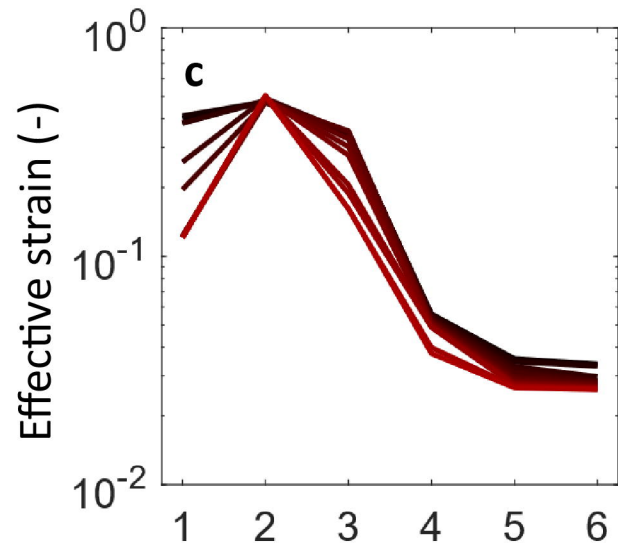
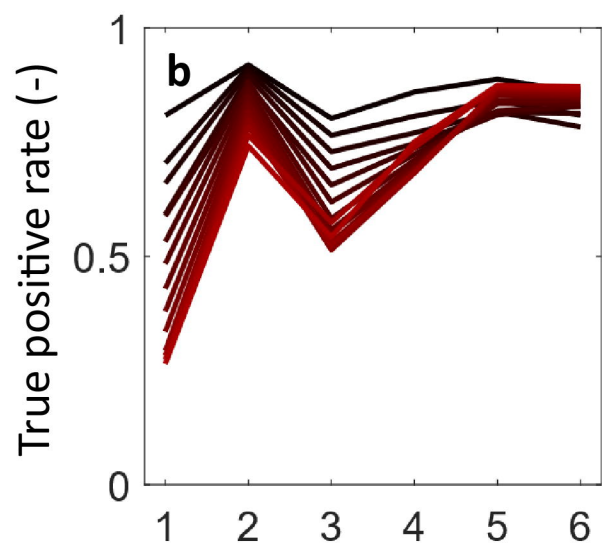
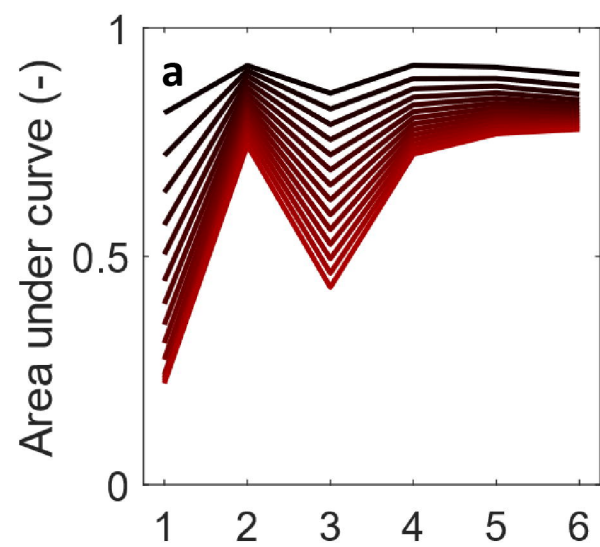
548

549



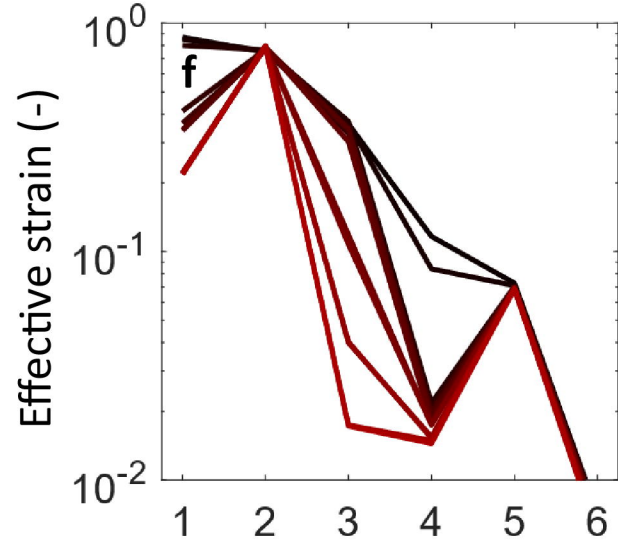
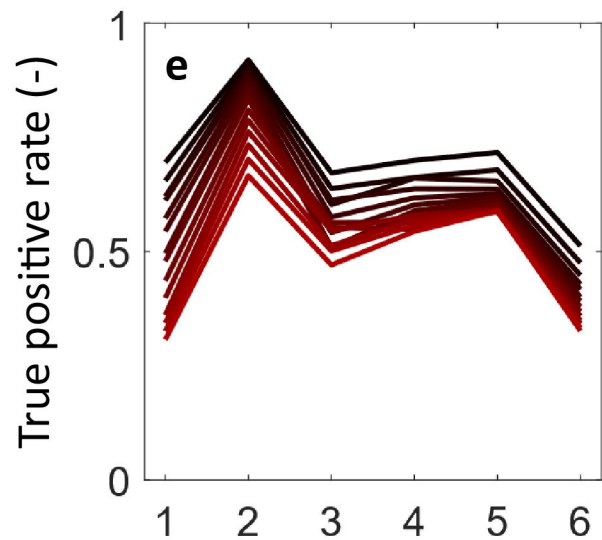
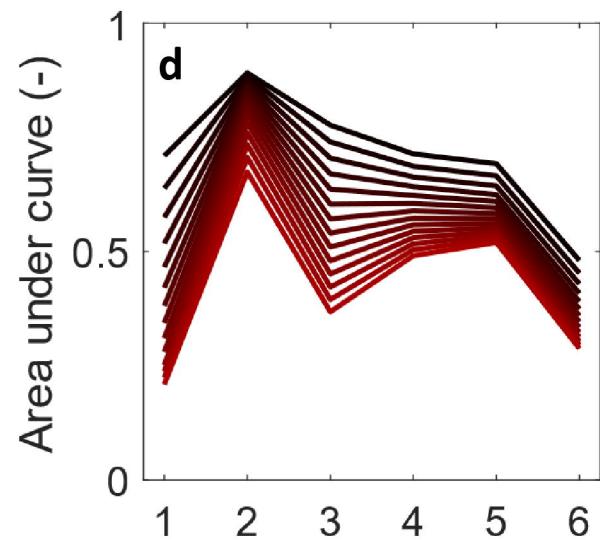


0.85 mm

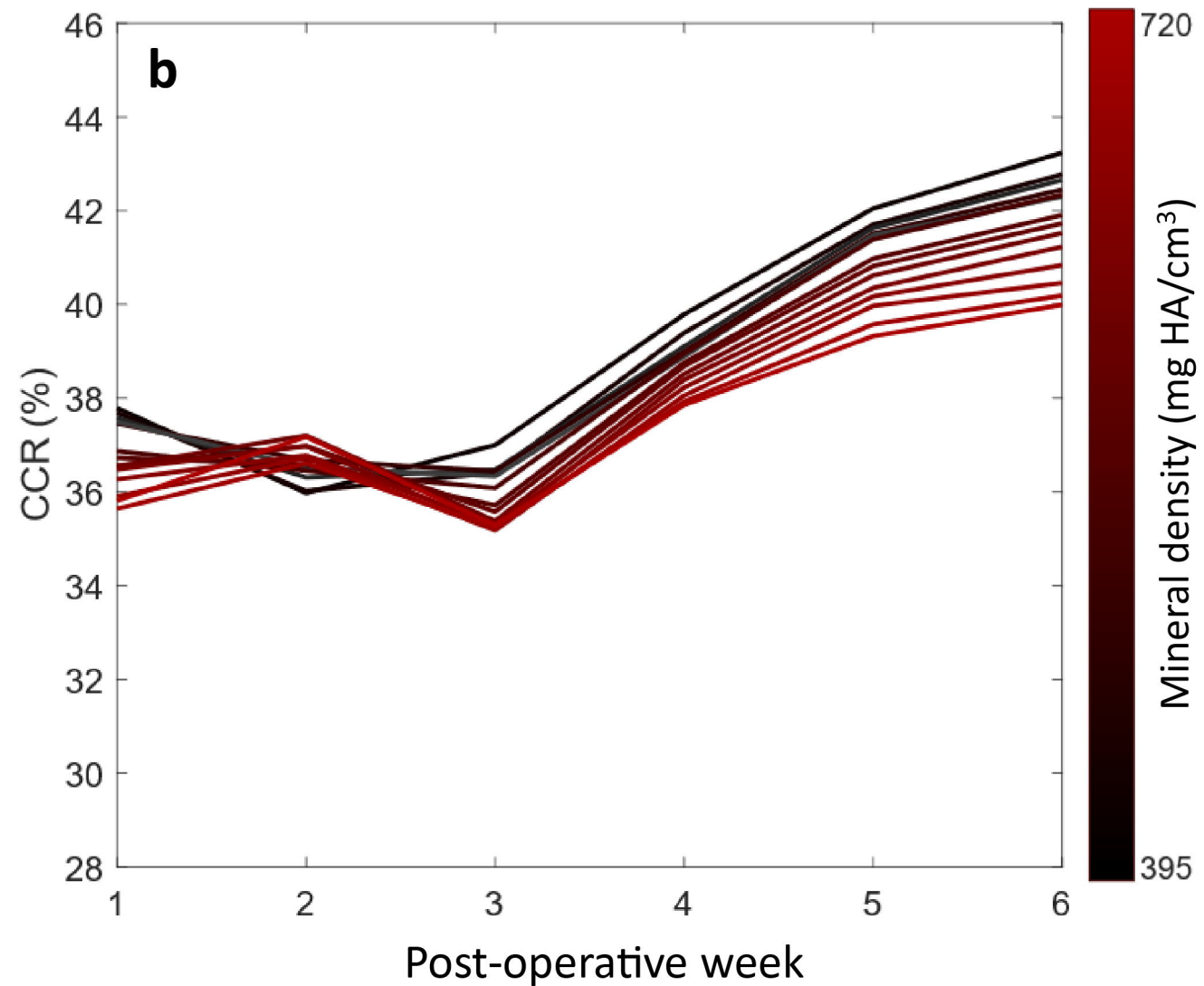
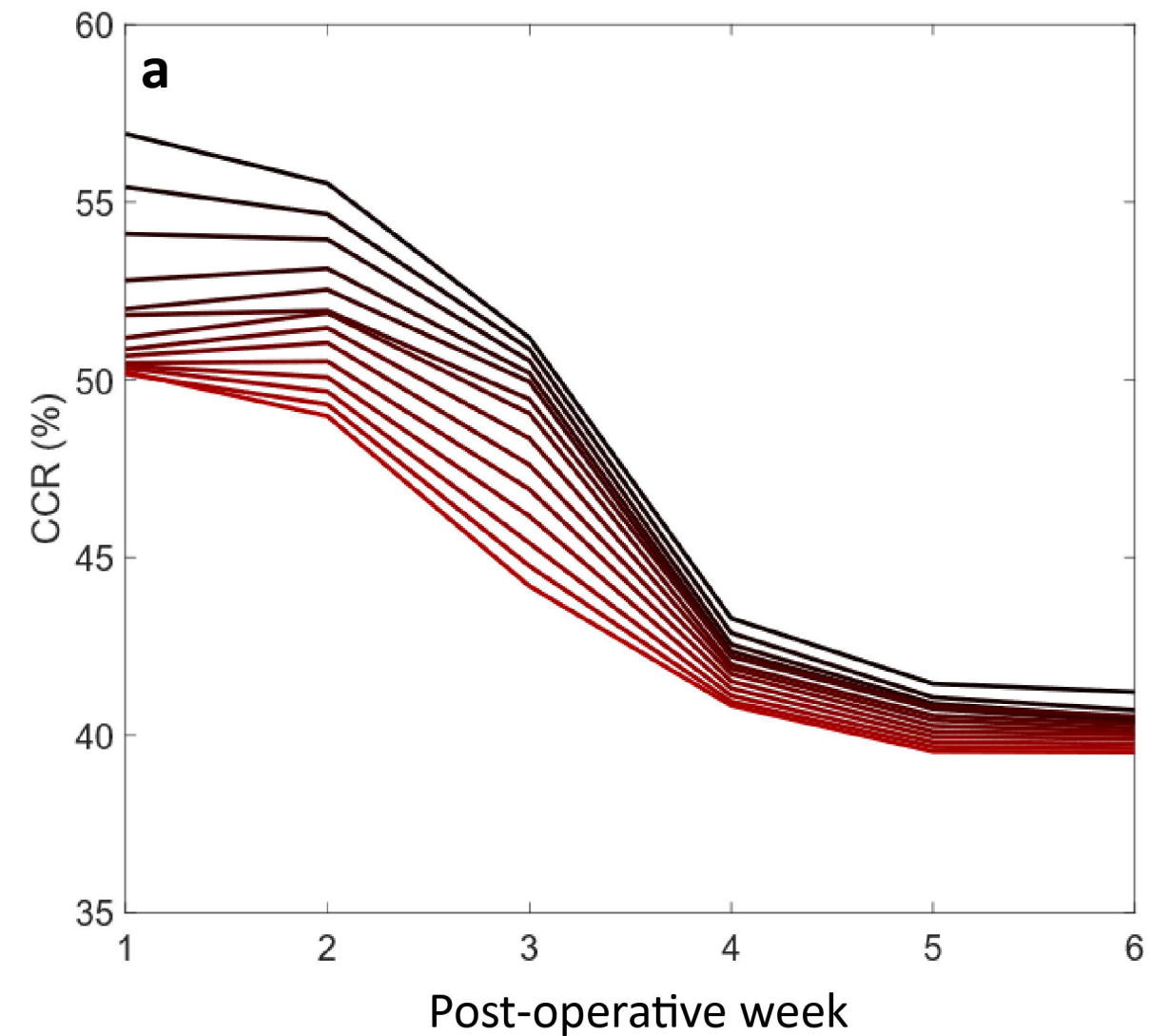


Mineral density (mg HA/cm³)

1.45 mm

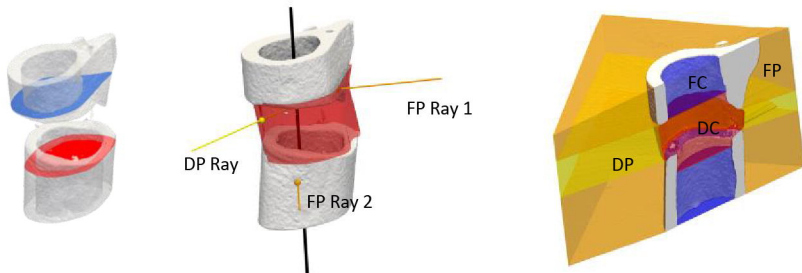
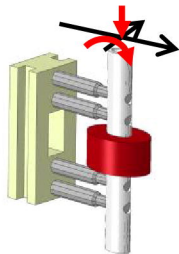
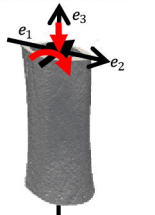


Post-operative week

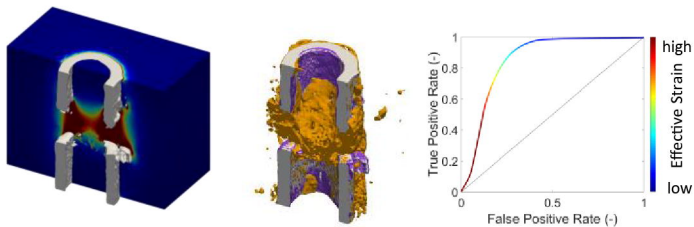


a

Defining volumes of interest

**b** Boundary conditions**c**

Mechanoregulation in the soft tissue

**d**

Mechanoregulation of surface remodelling

